Fourier Analysis and Loss Modeling for Inductive Wireless Electric Vehicle Charging with Reduced Stray Field

Andrew Foote, *Student Member, IEEE,* Daniel Costinett, *Senior Member, IEEE,* Ruediger Kusch, *Senior Member, IEEE,* Mostak Mohammad, *Senior Member, IEEE,* and Omer Onar, *Senior Member, IEEE*

Abstract

With the growth of electric vehicle (EV) popularity, different charging options to increase user convenience and reduce charging times are being considered and researched. Among these, high-power inductive wireless power transfer (WPT) systems for EVs are being designed to meet specifications such as stray field, power level, efficiency, misalignment tolerance, and ground clearance, which are all heavily influenced by the coil geometry. The proposed Fourier Analysis Method (FAM) is an analytical method to directly design coil geometries to meet stray field and power level requirements through an optimization of Fourier basis function coefficients. The outputs of the optimization are complex, planar coil potentials that meet the power level and stray field constraints with minimum current. Contours of these potentials determine the coil conductor paths and loss models predict the system efficiency and performance over misalignment. A 6.6 kW prototype WPT system with low stray field and high efficiency is built from the optimization results to validate the models and showcase the usefulness of the FAM design approach.

Index Terms

wireless power transfer, inductive power transmission, coil design, electric vehicles, Fourier analysis

Andrew Foote is the corresponding author of this work. Email: afoote5@vols.utk.edu; Phone: +1-650-496-7047; Mailing Address: 2704 Cherokee Farm Way, Knoxville, TN 37920 USA

Parts of this work were first published in IEEE COMPEL 2020 [1]. This paper significantly adds to the previous publication by detailing loss and misalignment models validating experimentally with a new 6.6kW coil.

This work made use of the Engineering Research Center Shared Facilities supported by the Engineering Research Center Program of the National Science Foundation and DOE under NSF Award Number EEC-1041877 and the CURENT Industry Partnership Program. Any opinions, findings and conclusions or recommendations expressed in this material are those of the authors and do not necessarily reflect those of the National Science Foundation.

This manuscript has been co-authored by Oak Ridge National Laboratory, operated by UT Battelle, LLC, under Contract No. DE-AC05-00OR22725 with the U.S. Department of Energy. The United States Government retains and the publisher, by accepting the article for publication, acknowledges that the United States Government retains a non-exclusive, paid up, irrevocable, world-wide license to publish or reproduce the published form of this manuscript, or allow others to do so, for United States Government purposes. The Department of Energy will provide public access to the results of federally sponsored research in accordance with the DOE Public Access Plan (http://energy.gov/downloads/doe-public access-plan).

I. Introduction

Inductive wireless power transfer (WPT) is useful in a variety of applications including the automotive and transportation sectors. The WPT systems have been proposed as a safe, convenient, flexible, and efficient charging solution that can easily be automated. The design of WPT systems to meet specifications such as power level, coupling, airgap, misalignment tolerance, stray field, and efficiency requires the computation of the fields, coupling, and inductances of various coil geometries. In particular, meeting the 27 μT ICNIRP 2010 public exposure magnetic field limit at the nominal WPT frequency of 85 kHz [2] and radiated EMI field limits in CISPR 11 [3] depends heavily on the coil geometry. More complex coil geometries such as bipolar coils and coils with shielding turns have been demonstrated to achieve higher power levels under stray field limits [4], [5]. Integrating shielding turns into the coil geometry design has several advantages over adding conductive or magnetic materials around the coil area to reduce stray field. In [6], [7], many Litz wire shielding turn designs were more efficient than copper ring shields or shielding plates of aluminum. In [8], eddy-current shielding with aluminum sheets was shown to actually increase the stray field for bipolar coil geometries. Likewise, adding ferrite teeth [9], aluminum sheets, or ferrite outside the coil geometry [8] decreases the mechanical airgap of the system or increases the effective coil area and weight.

Attempting to consider a wider range of coil geometries including shielding turns, as well as other design parameters such as ferrite thicknesses, number of turns, and conductor types, results in a large design space. With the rising number of iterations needed, optimization with FEA-based methods that rely on brute-force iterations with full or partial 3D-modeling similar to [4] become increasingly computationally expensive. Likewise, many analytical methods like [5], [6] are pertinent only to circular or rectangular coils and are not general enough to model a large variety of possible geometries and aspect ratios. This limitation is also present in ferrite [10] and external proximity effect loss models [11].

To address these issues, this work applies Fourier analysis to WPT coil design and loss modeling. Magnetic component modeling and optimization using Fourier basis functions is already well known in the design of magnetic resonance imaging (MRI) gradient coils [12], [13], fusion devices [14], and electric machines [15], [16]. In the field of wireless power transfer, Fourier analysis has been used to analytically calculate fields and mutual inductance of coils, but not to optimize coil designs and calculate losses. In [17], it is used to analyze circular and rectangular filament coils backed by magnetic or conductive media and predict mutual inductance. Similar modeling is used to model closely spaced rectangular coils in [18]. This work applies Fourier analysis to optimize the coil geometry as first published in [1] and adds loss and misalignment models experimentally validated with a 6.6 kW prototype.

The remainder of this work is organized as follows: Section II details the Fourier Analysis Method (FAM) for coil design optimization. Section III describes a misalignment model for translational and rotational misalignment and the application of loss models to the FAM including external proximity effect, ferrite losses, and others. To validate these models, the experimental results of a 6.6 kW prototype are given in Section IV. Finally, comparisons of this prototype with the literature are summarized in Table VI and conclusions are given in Section V.

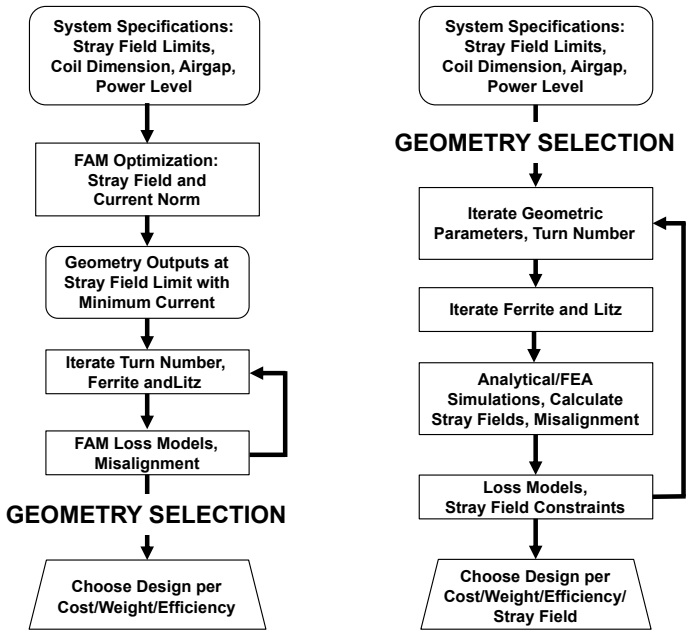

Fig. 1. Comparison of the Fourier Analysis Method (FAM) design process and a conventional design process. (a) The FAM design process where complex coil geometries are generated to meet the stray field limit with minimum current. The number of turns and coil materials are then iterated to evaluate loss for the candidate geometries. (b) A conventional design process [4], [5], [6] where geometric parameters are chosen and swept using FEA or analytical methods. Each parameter combination is evaluated for stray field and loss.

II. The Fourier Analysis Method

The Fourier Analysis Method (FAM) is an analytical method to directly design coil geometries through an optimization of Fourier basis function coefficients to meet specifications such as power level, coil dimension, and stray field. The use of Fourier basis functions allows for the rapid computation of the currents, field, and coupling of a wide range of symmetric coil shapes. The outputs of the optimization are the magnetic scalar potentials of coil geometries bounded to specified dimensions that meet the power and stray field constraints at given distances with minimum current. This first optimization step of the FAM design process in Fig. 1(a) is an inverse design step that directly optimizes the coil geometry to meet the input stray field limits with minimum current. The optimization outputs are then used to flexibly determine coil conductor paths and adjust the impedance of the coils for varying numbers of turns without changing the overall coil shape. Afterwards, losses are calculated for combinations of the number of turns, Litz wire type, ferrite thickness and misalignment. This is different from most conventional design methods [4], [5], [6] in Fig. 1(b) that sweep over geometric parameters and evaluate the stray field and loss of each combination.

The overall WPT system layout used in FAM is illustrated in Fig. 2 where the outer dimensions of the primary and secondary coils are x_{ext} and y_{ext}, the outer dimensions of the region for stray-field measurement are x_{meas} and y_{meas}, and the magnetic scalar potential is Ψ. In the FAM, the four different basis functions are combinations of cosine and sine functions in the x and y directions. Examples of the four selected functions, $\cos x \cos y$, $\sin x \cos y$,

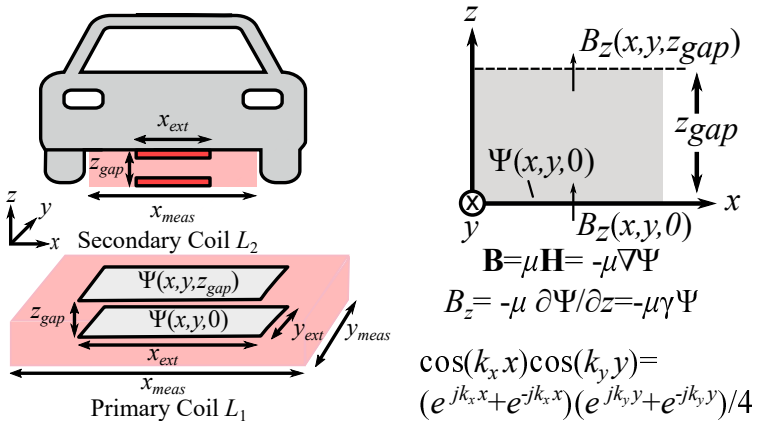

(a) (b)

Fig. 2. (a) Illustration of the EV WPT system defined by coil outer dimensions of x_{ext} and y_{ext}, system airgap z_{gap}, stray field limits outside a region with dimensions of x_{meas} and y_{meas}, and magnetic scalar potential Ψ used in the Fourier Analysis Method (FAM). (b) FAM axes layout and key equations.

$\cos x \sin y$, and $\sin x \sin y$, are shown in Fig. 3. As first detailed in [1], each function is defined by k_x and k_y, the spatial wavenumbers in units of radians per meter in the x and y-directions, respectively. The coefficients of the four basis functions are a $N \times N \times 4$ matrix with each $N \times N \times 1$ matrix representing the first quadrant of each of the basis function sets with coefficients $\psi(k_x, k_y)$. To compute the full Fourier-domain matrix of the coil shape, each $N \times N \times 1$ matrix is reflected according to the symmetry conditions of Fig. 3(a) to create a $(2N-1) \times (2N-1)$ matrix. This matrix is the DFT of the coil magnetic scalar potential,

$$\Psi(x,y,z) = \sum_{m=1}^{2N-1} \sum_{n=1}^{2N-1} \psi(k_x,k_y) e^{j(k_x x + k_y y + k_z z)}/4. \tag{1}$$

For ferrite-backed coils, the potential of the coil surface is defined by the surface current boundary condition

$$\boldsymbol{K} = \nabla \times \hat{k}\Psi = \frac{\partial \Psi}{\partial y}\hat{\imath} - \frac{\partial \Psi}{\partial x}\hat{\jmath} \tag{2}$$

where $\hat{\imath}$, $\hat{\jmath}$, and $\hat{k}$ are unit vectors in the x, y, and z directions, respectively. This assumes the change in the magnetic potential and field in the ferrite are close to zero due to the low reluctance of the ferrite compared to the airgap. The surface currents in the x and y-direction, K_x and K_y, are then

$$K_x(x,y,0) = \sum_{m=1}^{2N-1} \sum_{n=1}^{2N-1} jk_y \psi(k_x,k_y) e^{j(k_x x + k_y y)}/4 \tag{3}$$

$$K_y(x,y,0) = \sum_{m=1}^{2N-1} \sum_{n=1}^{2N-1} -jk_x \psi(k_x,k_y) e^{j(k_x x + k_y y)}/4. \tag{4}$$

This surface current representation allows for the coil geometry to be analyzed as a surface current density with less dependence on the number of turns. To determine the coil conductor paths and current, the surface currents are grouped by dividing the net change of potential into a number of turns N_T. The number of turns can be adapted

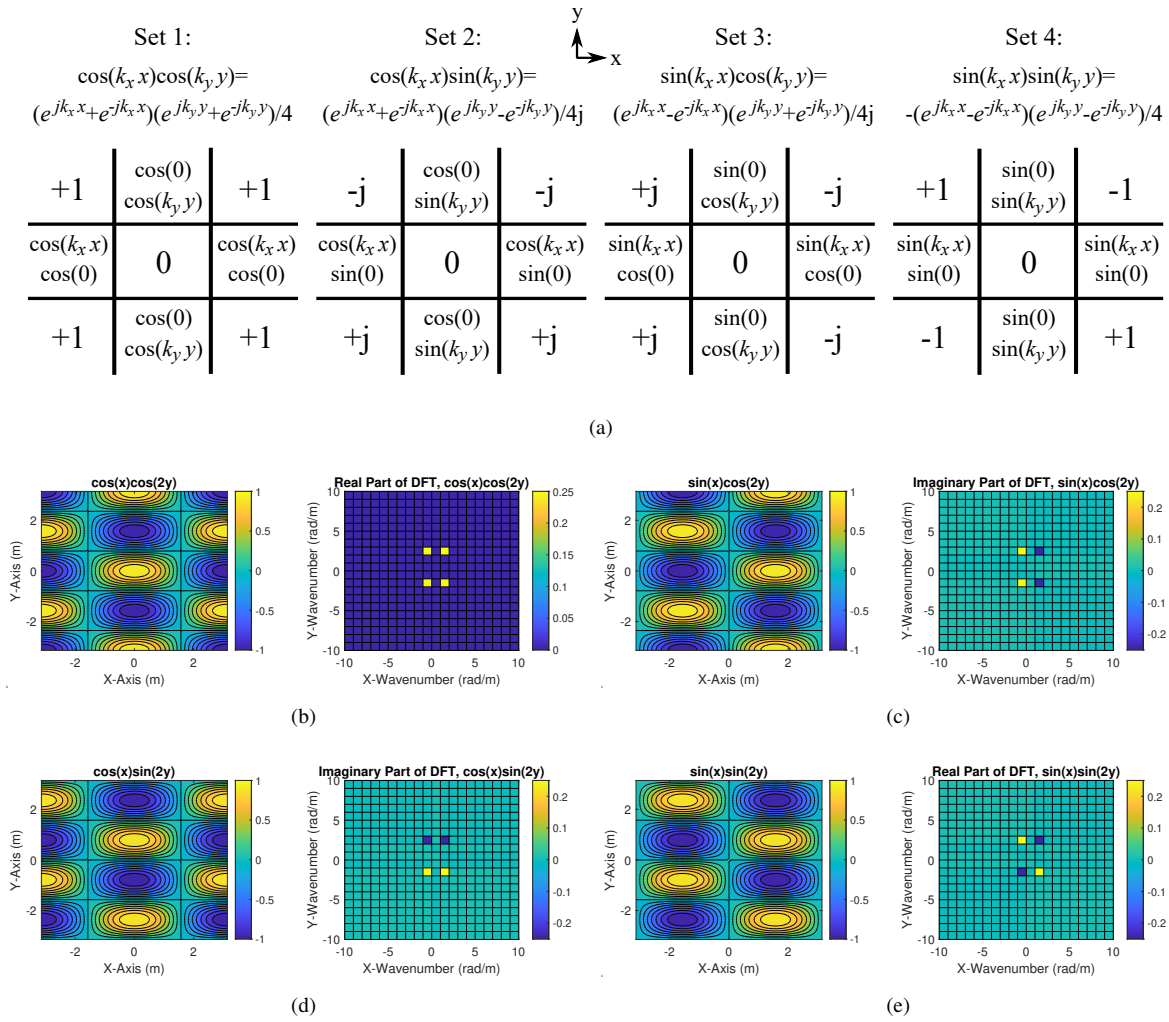

Fig. 3. Diagrams of the 4 basis functions sets considered in the Fourier Analysis Method. (a) The symmetry conditions for each basis function set comprised of real and complex conjugate relationships. With these relationships, each basis function can be represented by one value in the first quadrant, limiting the number of variables and constraints needed in the optimization function. (b) Example of a $\cos x \cos y$ basis function. (c) Example of a $\sin x \cos y$ basis function. (d) Example of a $\cos x \sin y$ basis function. (e) Example of a $\sin x \sin y$ basis function.

to flexibly change the impedance of the coils to meet various driving voltages and loads. This results in the RMS current in each turn: I_1 for the primary or I_2 for the secondary,

$$I_1 = (\max \Psi(x, y, 0) - \min \Psi(x, y, 0))/N_T. \tag{5}$$

The conductor paths are the contours of the potential at values

$$C = \min \Psi(x, y, 0) + \left(0 : (N_T - 1) + \frac{1}{2}\right) I_1. \tag{6}$$

As in [1], the number of turns are limited by the outer diameter of the gauge of wire, d_{out}, and the maximum current density, K_{max}, by

$$\frac{\max \Psi(x, y, 0) - \min \Psi(x, y, 0))}{N_T d_{out}} = \frac{I_1}{d_{out}} < K_{max} \tag{7}$$

so that the geometries fit in a single winding layer.

In the Fourier domain, the potential Ψ is differentiated to obtain algebraic relationships between the potential and the field $\boldsymbol{B}$,

$$\boldsymbol{B} = \mu_0 \boldsymbol{H} = -\mu_0 \nabla \Psi. \tag{8}$$

Neglecting displacement current in quasi-magnetostatic conditions, the wavenumber in the z-direction, k_z, is derived by observing that $\nabla \times \boldsymbol{B} = 0$ in the absence of airgap currents. Here, it is assumed there are no conductors or volume currents between the primary and secondary coils with only air in the airgap. Combined with $\nabla \cdot \boldsymbol{B} = 0$, the field and potential satisfy

$$\nabla^2 \Psi = \nabla^2 \boldsymbol{B} = 0. \tag{9}$$

Therefore, when real, non-zero wavenumbers exist in the x and y-directions, k_z is imaginary and is

$$k_z = \pm\sqrt{-k_x^2 - k_y^2} = \pm j\gamma, \tag{10}$$

where $\gamma = \sqrt{k_x^2 + k_y^2}$, and the magnetic potential in the airgap must satisfy

$$\frac{\partial^2 \Psi}{\partial z^2} - k_z^2 \Psi = 0 \tag{11}$$

which has solution

$$\Psi(z) = c_1 e^{-\gamma z} + c_2 e^{\gamma z}. \tag{12}$$

The constants c_1 and c_2 are found using the boundary conditions at $\Psi(0)$ and $\Psi(z_{gap})$, yielding the relationship [15],

$$\Psi(z) = \frac{\sinh \gamma z}{\sinh \gamma z_{gap}} \Psi(z_{gap}) - \frac{\sinh \gamma (z - z_{gap})}{\sinh \gamma z_{gap}} \Psi(0). \tag{13}$$

By combining (8) with (13), the fields at z are a function of z_{gap} and γ for ferrite-backed coils with single-sided flux generation

$$B_x(x,y,z) = \sum_{m=1}^{2N-1} \sum_{n=1}^{2N-1} \frac{-\mu_0 j k_x \psi(k_x,k_y) e^{j(k_x x + k_y y)}}{4} \cdot \frac{\sinh \gamma (z - z_{gap})}{\sinh \gamma z_{gap}} \tag{14}$$

$$B_y(x,y,z) = \sum_{m=1}^{2N-1} \sum_{n=1}^{2N-1} \frac{-\mu_0 j k_y \psi(k_x,k_y) e^{j(k_x x + k_y y)}}{4} \cdot \frac{\sinh \gamma (z - z_{gap})}{\sinh \gamma z_{gap}} \tag{15}$$

$$B_z(x,y,z) = \sum_{m=1}^{2N-1} \sum_{n=1}^{2N-1} \frac{-\mu_0 \gamma \psi(k_x,k_y) e^{j(k_x x + k_y y)}}{4} \cdot \frac{\cosh \gamma (z - z_{gap})}{\sinh \gamma z_{gap}}. \tag{16}$$

This calculation determines the fields from the primary coil only with $\Psi(z_{gap}) = 0$ and zero tangential field at the surface of the secondary ferrite. The fields from the secondary coil are calculated in a similar manner and can be added to the primary fields in the air gap by superposition.

By (9)–(16), coils with potentials with higher k_x and k_y, i.e. with shorter wavelengths, will generate fields that decay faster in the z-direction than those with smaller k_x and k_y. This scattering relationship describes how coils with larger diameters have fields that decay slower away from the coil surface than those of smaller coils. An example of this for a rectangular primary coil is shown in Fig. 4. At the surface of the coil, the DFT of the potential and discretized potential are shown in Fig. 4(a)-4(b). The z-field at the surface of the coil by (16) is

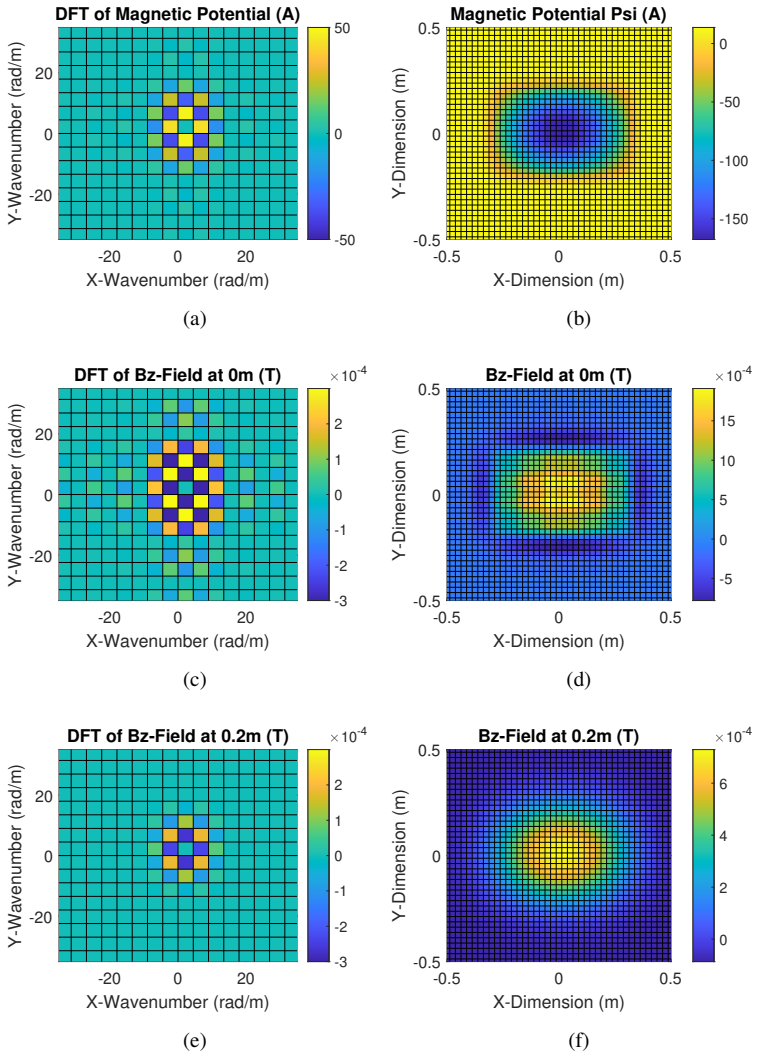

Fig. 4. Example potentials and field of a rectangular coil when $z_{gap} = 0.2$ m. (a) DFT and (b) contours of the magnetic scalar potential. (c) DFT and (d) discretized surface z-field at the surface of the primary coil. (e) DFT and (f) discretized z-field of the primary coil across the airgap at the surface of the secondary coil.

Fig. 4(c)-4(d). The z-field from the primary at the surface of the secondary at z_{gap} is Fig. 4(e)-4(f), where only the low-frequency components of the field are largely remaining. The average of the fields in the airgap are also conveniently obtained by this representation. The average field is derived by integrating the contribution from each basis function from $z = 0$ to z_{gap} and dividing by z_{gap} to obtain the average field in the airgap,

$$B_{x,avg}(x,y) = \sum_{m=1}^{2N-1}\sum_{n=1}^{2N-1} \frac{-\mu_0 j k_x \psi(k_x,k_y) e^{j(k_x x + k_y y)}}{\gamma z_{gap} \sinh \gamma z_{gap}} \cdot (\cosh \gamma z_{gap} - 1) \tag{17}$$

$$B_{y,avg}(x,y) = \sum_{m=1}^{2N-1}\sum_{n=1}^{2N-1} \frac{-\mu_0 j k_y \psi(k_x,k_y) e^{j(k_x x + k_y y)}}{\gamma z_{gap} \sinh \gamma z_{gap}} \cdot (\cosh \gamma z_{gap} - 1) \tag{18}$$

$$B_{z,avg}(x,y) = \sum_{m=1}^{2N-1}\sum_{n=1}^{2N-1} \frac{-\mu_0 \gamma \psi(k_x,k_y) e^{j(k_x x + k_y y)}}{\gamma z_{gap}}. \tag{19}$$

The average field magnitude in the airgap, $B_{avg}(x,y)$, is then

$$B_{avg}(x,y) = \sqrt{B_{x,avg}(x,y)^2 + B_{y,avg}(x,y)^2 + B_{z,avg}(x,y)^2}. \tag{20}$$

The computation of the field at the surface of the coils allows for the computation of the coupling coefficient as detailed in [1] assuming matched couplers and currents

$$k = \frac{E_m(\psi)}{2E_s(\psi)} = \frac{MI_1I_2}{\frac{1}{2}L_1I_1^2 + \frac{1}{2}L_2I_2^2} = \frac{\int_\Omega \Psi(x,y,0)B_z(x,y,z_{gap})d\Omega}{\int_\Omega \Psi(x,y,0)B_z(x,y,0)d\Omega}. \tag{21}$$

A. Optimization of Stray Field and Current

Using the FAM, an optimization is formulated and solved to design coil geometries to minimize the total current for a fixed power level when bounded by coil extents at x_{ext} and y_{ext} and field limits at the measurement extents x_{meas} and y_{meas}. The objective function is formulated as the minimization of the surface integral of the total current in the coil structure squared, $\int_\Omega K(x,y,0)^2 d\Omega$. The surface integral

$$\int_\Omega K(x,y,0)^2 d\Omega = (||K_x(\psi)||_2^2 + ||K_y(\psi)||_2^2)/16 \tag{22}$$

is calculated by noting that the Fourier transform is a unitary function. This avoids the computation of $K(x,y,0)$ in each objective function evaluation step. The 1-norm of the magnitude of the basis function coefficients is added to eliminate small values of zero-valued basis functions such as $\sin 0 \cos y$ yielding the objective function

$$\frac{||K_x(\psi)||_2^2 + ||K_y(\psi)||_2^2}{16P} + \alpha\frac{||\psi||_1}{P} \tag{23}$$

where $\alpha = 0.1$. The first constraint is the coil-coil power transfer

$$(P - 2\pi f E_m(\psi))/P \leq 0. \tag{24}$$

The next constraint is the maximum average stray field magnitude $B_{str,lim}$ outside the measurement extents x_{meas} and y_{meas},

$$(||B_{str,avg}(x,y)||_{50} - B_{str,lim})/B_{str,lim} \leq 0. \tag{25}$$

The inclusion of the stray field as a constraint weights the compliance of the system with safety standards for public magnetic field exposure. This is computed as the 50-norm of the spatial stray-field matrix which approximates the infinity norm or the maximum magnitude of the matrix. $B_{str,avg}$ is the average field magnitude B_{avg} outside the measurement extents x_{meas} and y_{meas}.

The third constraint limits the current density to the desired coil extents x_{ext} and y_{ext} such that the surface integral of the stray current squared, $\int_\Omega K_{str}(x,y,0)^2 d\Omega$, is a small percentage, $\beta = 10^{-4}$, of the surface integral of the total current $\int_\Omega K(x,y,0)^2 d\Omega$.

$$\frac{\int_\Omega K_{str}(x,y,0)^2 d\Omega - \beta\int_\Omega K(x,y,0)^2 d\Omega}{\int_\Omega K(x,y,0)^2 d\Omega} \leq 0 \tag{26}$$

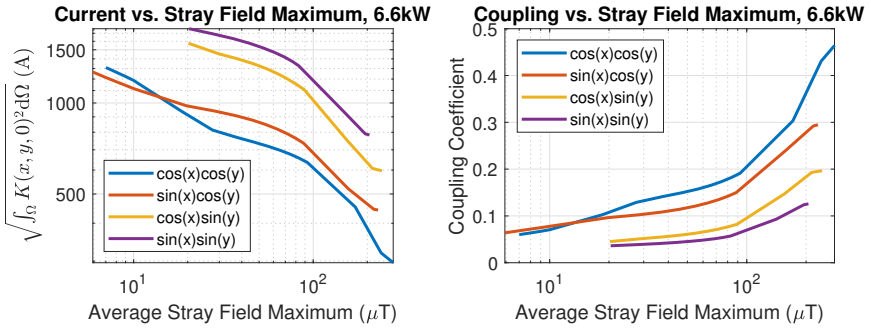

(a) (b)

Fig. 5. Optimization Outputs: (a) The maximum average stray field magnitude vs. the square root of the integral of the current magnitude squared at 6.6 kW and (b) coupling coefficient at $z_{gap} = 200$ mm at alignment for $x_{ext} = 0.7$ m and $y_{ext} = 0.5$ m for $B_{str,lim}$ of 5 μT to 1 mT with $x_{meas} = 0.8$ m and $y_{meas} = 0.6$ m.

In summary, the objective function and constraints form the optimization

$$\min \left(\frac{||K_x(\psi)||_2^2 + ||K_y(\psi)||_2^2}{16P} + \alpha \frac{||\psi||_1}{P} \right)$$

s.t.

$$\begin{aligned} (P - 2\pi f E_m(\psi))/P &\leq 0, \\ (||B_{str,avg}(x,y)||_{50} - B_{str,lim})/B_{str,lim} &\leq 0, \\ \frac{\int_\Omega K_{str}(x,y,0)^2 d\Omega - \beta \int_\Omega K(x,y,0)^2 d\Omega}{\int_\Omega K(x,y,0)^2 d\Omega} &\leq 0. \end{aligned} \tag{27}$$

As first given in [1], the results of this optimization are plotted in Fig. 5 for $B_{str,lim}$ of 5 μT to 1 mT with $x_{ext} = 0.7$ m and $y_{ext} = 0.5$ m, and with $x_{meas} = 0.8$ m and $y_{meas} = 0.6$ m. In these results, as $B_{str,lim}$ is reduced, the coupling of the geometries decreases and the required current to achieve the 6.6 kW power level increases for the fixed coil extents and airgap.

Contours of the outputs at $B_{str,lim} = 20$ μT and 1 mT are shown in Fig. 6. As shown, when $B_{str,lim} = 1$ mT in the geometries are simple rectangular, bipolar or double-D, and quadrupole shapes limited by the extents of the coil in Fig. 6(a)-6(d). When constrained by $B_{str,lim} = 20$ μT, the geometries develop smaller poles and shielding structures that provide flux cancellation to reduce the field outside the stray field boundaries in Fig. 6(e)-6(h). The smaller poles reduce the coupling of the coils for the fixed airgap. Likewise, the shielding structures do not contribute significantly to the power transfer and require additional current. These two factors increase the amount of current needed for a given amount of power for Fig. 6(e)-6(h) relative to the simpler structures of Fig. 6(a)-6(d).

III. Misalignment and Loss Modeling

Using the output geometries derived from the optimization for a given $B_{str,lim}$ constraint, the loss and misalignment models detailed in this work are used to analyze efficiency for various conductor types, ferrite thicknesses,

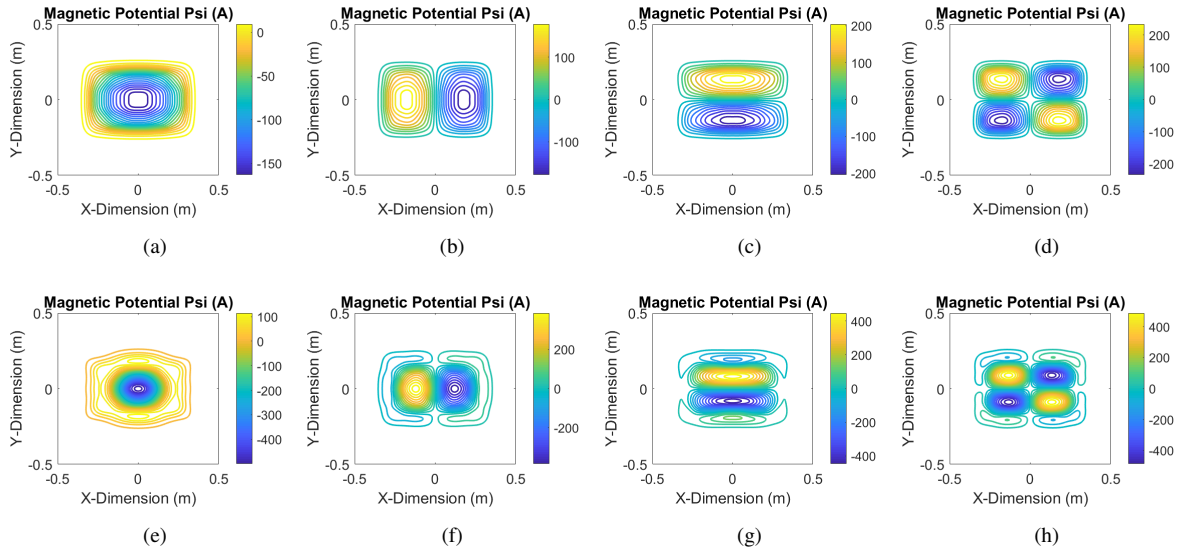

Fig. 6. Plots of coil contours from each basis function for $x_{ext} = 0.7$ m and $y_{ext} = 0.5$ m when constrained by $B_{str,lim} = 1$ mT with $x_{meas} = 0.8$ m and $y_{meas} = 0.6$ m with a number of turns $N_T = 20$. (a) A rectangular coil from the $\cos x \cos y$ set. (b) A bipolar coil in the x-direction from the $\sin x \cos y$ set. (c) A bipolar coil in the y-direction from the $\cos x \sin y$ set. (d) A 4-pole coil from the $\sin x \sin y$ set. Plots when constrained by $B_{str,lim} = 20$ µT with a number of turns $N_T = 24$. (e) A shielded rectangular coil from the $\cos x \cos y$ set. (f) A shielded bipolar coil in the x-direction from the $\sin x \cos y$ set. (g) A shielded bipolar coil in the y-direction from the $\cos x \sin y$ set. (h) A shielded quadrupole coil from the $\sin x \sin y$ set.

and number of turns. As an example, the two geometries in Fig. 7(a)-7(b) are selected for further analysis. These are the optimization outputs where $B_{str,lim} = 100$ µT for the $\cos x \cos y$ and the $\sin x \cos y$ basis functions. By varying the number of turns, the impedance of the coils is tuned to meet input voltage requirements with series-series compensation in Fig. 7(c)-7(d). Using the loss models, the efficiencies at alignment are given in Fig. 7(e)-7(f). Here, more turns with higher voltages and lower currents are more efficient than having fewer turns with higher currents mostly due to the reduction of switching device conduction losses as a function of current. Here, it is assumed that the inverter and rectifier have constant device on-state resistances and forward voltages. Solutions with thicker gauges of wire and higher turns are limited by (7) so that the conductors fit in a single layer.

A. *Misalignment Model*

The FAM can predict the system performance over both translational and rotational misalignments by calculating the fields and mutual inductance of the system for misaligned conditions. For example, the efficiency over misalignment of the geometries of Fig. 7(a)-7(b) are given in Fig. 7(g)-7(h). In the Fourier domain, translational misalignment is modeled by adding phase-shift to the Fourier components, where x_{sft} and y_{sft} are the translational misalignment of the coil in the x-direction and y-direction respectively,

$$\psi_{sft}(k_x, k_y) = \psi(k_x, k_y) e^{(-k_x x_{sft} - k_y y_{sft})}. \tag{28}$$

An example of this operation for the selected geometry potential in Fig. 8(a) is shown in Fig. 8(c).

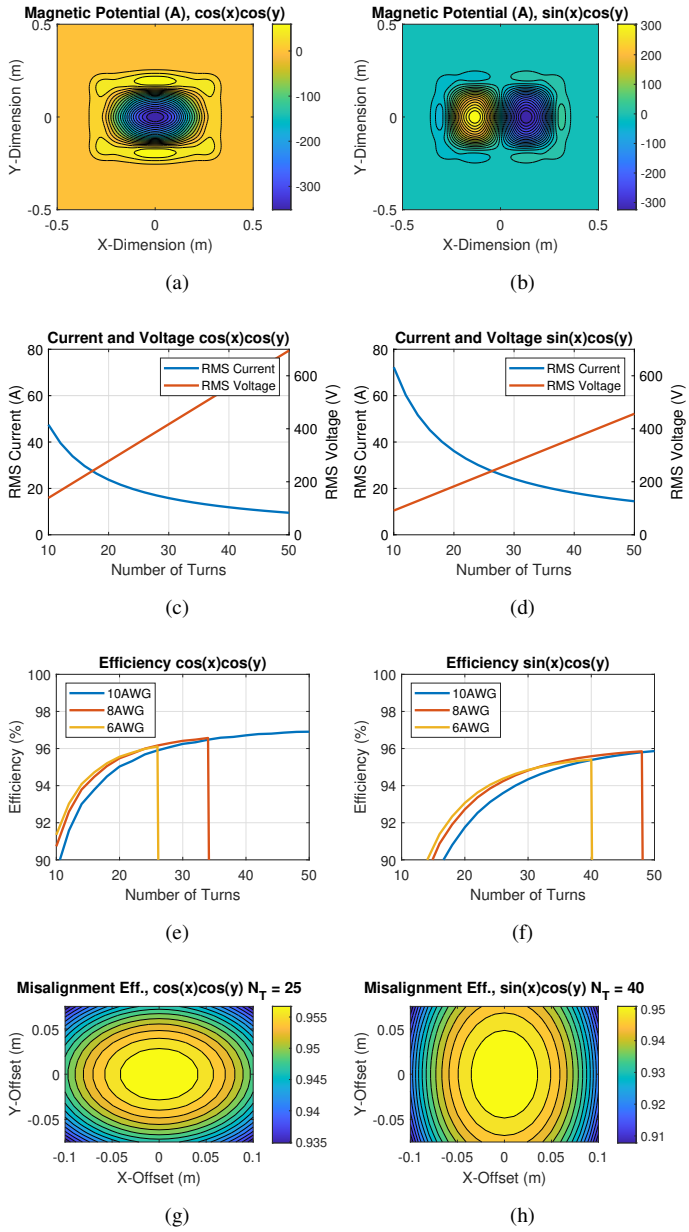

Fig. 7. Points from the optimization where $B_{str,max} = 100\mu$T shown when $f = 85$ kHz, and $z_{gap} = 210$ mm, and $P = 6.6$ kW and modeled loss using the parameters of Table I. (a) Potential of the $\cos x \cos y$ coil geometry. (b) Potential of the $\sin x \cos y$ coil geometry. (c) Current and voltage for the (c) $\cos x \cos y$ coil geometry and the (d) $\sin x \cos y$ coil geometry. Efficiency at alignment of the (e) $\cos x \cos y$ coil geometry and the (f) $\sin x \cos y$ coil geometry from the loss models in this paper where $I_1 = I_2$. Misalignment efficiency of the (g) $\cos x \cos y$ coil geometry with $N_T = 25$ and the (h) $\sin x \cos y$ coil geometry with $N_T = 40$ with $I_1 = I_2$.

In a similar manner, rotation in the spatial domain produces rotation in the Fourier domain,

$$\begin{bmatrix} k_x' \\ k_y' \end{bmatrix} = \begin{bmatrix} \cos\theta_{sft} & -\sin\theta_{sft} \\ \sin\theta_{sft} & \cos\theta_{sft} \end{bmatrix} \begin{bmatrix} k_x \\ k_y \end{bmatrix} \tag{29}$$

where θ_{sft} is the rotational misalignment. An example of this is shown in Fig. 8(b). Due to the limited number of

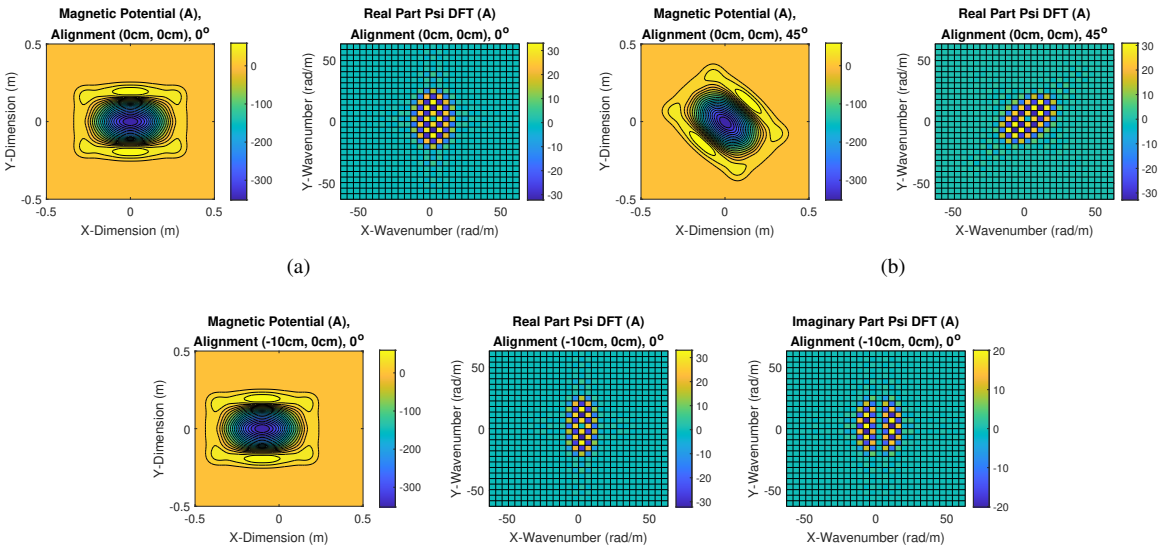

Fig. 8. Magnetic scalar potential under different misalignment cases. (a) Magnetic potential and DFT when aligned. (b) Magnetic potential and DFT with rotational misalignment of 45°. (c) Magnetic potential and DFT with translational misalignment of -10 cm in the x-direction.

basis functions used in the optimization, this operation is performed by taking the discrete Fourier transform of the rotated spatial domain potential, which has a finer discretization, to interpolate and determine the rotated Fourier components.

B. Coil Conduction Losses

As alternating current (AC) current flows through coupled transformer windings, the losses in the wire are

$$P_w = \frac{1}{2}\begin{bmatrix}\mathbf{I}_1 & \mathbf{I}_2\end{bmatrix}\begin{bmatrix}R_{11} & R_{12}\\ R_{21} & R_{22}\end{bmatrix}\begin{bmatrix}\mathbf{I}_1^*\\ \mathbf{I}_2^*\end{bmatrix} \tag{30}$$

where $\mathbf{I}_1$ and $\mathbf{I}_2$ are the current phasors of the primary and secondary coils respectively [19]. However, in inductive power transfer, the relative phase shift between the winding will be near 90° such that the mutual resistance terms, R_{12} and R_{21} are neglected. This leaves only the self-resistance of the coils, R_{11} and R_{22}.

The increase in self-resistance of a conductor carrying AC is comprised of two effects: the skin effect and the proximity effect. The skin effect is caused by the change in the magnetic field within the conductor due to the change in current within that wire as in Ampere's Law and is characterized by the skin depth

$$\delta_s = \sqrt{\frac{\rho}{\pi\mu f}} = \sqrt{\frac{2\rho}{\omega\mu}} \tag{31}$$

which is defined as the depth in which the field and current density in the conductor falls to e^{-1} of its initial value at the surface of a conductor with resistivity ρ and permeability μ when conducting AC at frequency $\omega = 2\pi f$.

Given the crowding of the current and the associated increase in current density, the skin depth is used in the calculation of the total AC resistance of WPT coil conductors due to the skin effect. For an individual circular conductor with a ratio of strand diameter d_{str} and skin depth δ_s the ratio $F_R(\zeta) = r_s/r_{DC}$ is

$$F_R = \frac{\zeta}{2\sqrt{2}} \left(\frac{\mathrm{ber}_0(\zeta)\mathrm{bei}_1(\zeta) - \mathrm{ber}_0(\zeta)\mathrm{ber}_1(\zeta)}{\mathrm{ber}_1(\zeta)^2 + \mathrm{bei}_1(\zeta)^2} - \frac{\mathrm{bei}_0(\zeta)\mathrm{ber}_1(\zeta) + \mathrm{bei}_0(\zeta)\mathrm{bei}_1(\zeta)}{\mathrm{ber}_1(\zeta)^2 + \mathrm{bei}_1(\zeta)^2} \right) \tag{32}$$

where

$$\zeta = \frac{d_{str}}{\sqrt{2}\delta_s} \tag{33}$$

as derived in [20], [21], where r_s is the AC resistance of a strand of wire including skin effect and r_{DC} is the DC resistance. Equation (32) is comprised of Kelvin functions that separate the real and imaginary parts of the value of Bessel functions of the first kind $\mathrm{J}_v(\cdot)$ of order v with argument complex argument $j^{3/2}x$ as in

$$\mathrm{J}_v(j^{3/2}x) = \mathrm{ber}_v(x) + j\,\mathrm{bei}_v(x). \tag{34}$$

Within a circular Litz wire cable, there are n conductors of diameter d_{str}. Once F_R is computed, the total resistance of the Litz wire including skin effect and DC-resistance, R_s, is

$$R_s = \left(\frac{r_{DC} \cdot F_R(\zeta)}{n} \right) L_T \cdot 1.015^{N_b} \cdot 1.025^{N_c} \tag{35}$$

where r_{DC} is the resistance of one strand in the Litz wire per unit length. Here L_T is the total length of wire in the coil multiplied by additional factors to account for the additional length of each conductor due to the number of bundling operations N_b and number of cabling operations N_c as given in the manufacturer datasheet [22].

Losses also occur due to the effect of external fields from conductors near each other, known as the proximity effect. For Litz wire, this is subdivided into two primary categories: internal proximity effect losses and external proximity effect losses. The increase of resistance from these two effects are governed by the factor G_R as defined in (36) which is a function of ζ derived in a similar fashion to F_R [20], [21].

$$G_R = -\frac{\zeta\pi^2 d_{str}^2}{\sqrt{2}} \left(\frac{\mathrm{ber}_2(\zeta)\mathrm{ber}_1(\zeta) + \mathrm{ber}_2(\zeta)\mathrm{ber}_1(\zeta)}{\mathrm{ber}_0(\zeta)^2 + \mathrm{bei}_0(\zeta)^2} + \frac{\mathrm{bei}_2(\zeta)\mathrm{bei}_1(\zeta) - \mathrm{bei}_2(\zeta)\mathrm{bei}_1(\zeta)}{\mathrm{ber}_0(\zeta)^2 + \mathrm{bei}_0(\zeta)^2} \right) \tag{36}$$

Internal proximity effect losses occur within Litz wire cables because the magnetic field generated from the total current within the cross section of the cable varies the distribution of current within individual strands, increasing radially from center of the cable. The strands are bundled and cabled to vary the position of each strand over the length of Litz wire. The external proximity effect is due to the effect of the total field of the coil on each section of a conductor. For ferrite-backed coils with a non-zero gap between the ferrite and windings, the external field $\vec{H_e}$ is the field on each section of the wire. The cross-product of this and the wire direction yields the field orthogonal to the winding section direction unit vector $\hat{dr}$. This includes all H_z components, as the coils are assumed to be in the x-y plane, and H_x and H_y components depending on the direction of the section of wire [11]. The fields are calculated by FAM by (14)-(16). The result of this line integration of the field along the coil contours of the wire is taken and normalized by the RMS current in the wire, I_1 or I_2, to yield the external proximity effect resistance. The summation of these two terms yields the total increase in resistance due to the proximity effect.

$$R_{prox} = n \cdot r_{DC} \cdot G_R(\zeta) \cdot 1.015^{N_b} \cdot 1.025^{N_c} \cdot \left(\oint |\vec{H_e} \times \hat{dr}|^2 / I_1^2 + \frac{1}{2\pi^2 d_o^2} L_T \right) \tag{37}$$

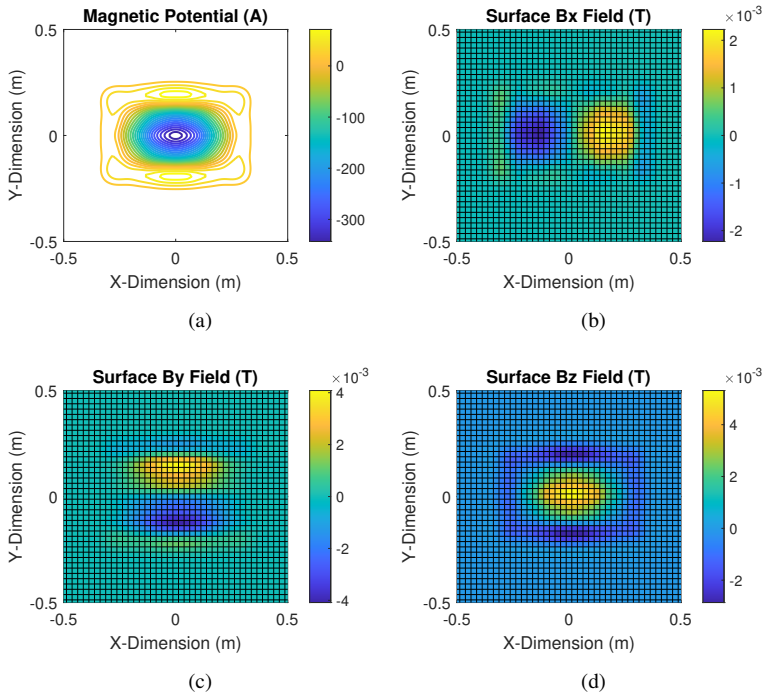

Fig. 9. Example of the coil contours and fields used to calculate external proximity effect loss in FAM. (a) Contours of the magnetic scalar potential of the prototype coil. Surface fields of the coil with a current of 17.3 A in the (b) x-direction, (c) y-direction, and (d) z-direction.

An example of the coil contours and fields used to compute (37) for $I_1 = 17.3$ A is given in Fig. 9. The external fields and direction of each section of wire are calculated with an interpolation of the field values calculated by the FAM to determine orthogonal field components. Once the resistance increases due to the skin effect and proximity effect are calculated, the total AC resistance of each coil at a given frequency, R_{11} and R_{22}, are found by the addition of R_s and R_{prox}.

Using this methodology, the AC resistance of Litz wire coils with complex geometries can be determined. In each case, the overall length of Litz wire and the total external proximity effect is conveniently determined by a line integral of the conductor contours. The orthogonal external fields along the contours are interpolated from the field calculations in (14)-(16) without the need for 3D FEA simulation.

C. Ferrite Losses

Losses in soft-magnetic materials are primarily broken down into hysteresis loss and conduction losses. However, the resistivity of ferrite materials is high, on the order of 5 Ωm, such that the eddy currents in the material are neglected. The Steinmetz equation

$$P_{fe} = C_m f^{\alpha} B_p^{\beta} (T_{fer}^2 C_{t2} - T_{fer} C_{t1} + C_{t0}) \tag{38}$$

is used as a curve-fit of hysteresis loss plots within certain ranges where C_m, α, and β are curve-fit coefficients, P_{fe} is the specific hysteresis loss of the material, and B_p is the peak flux density in the material. The Steinmetz equation is used as the coil currents and flux densities are highly sinusoidal and the flux densities in the ferrite are

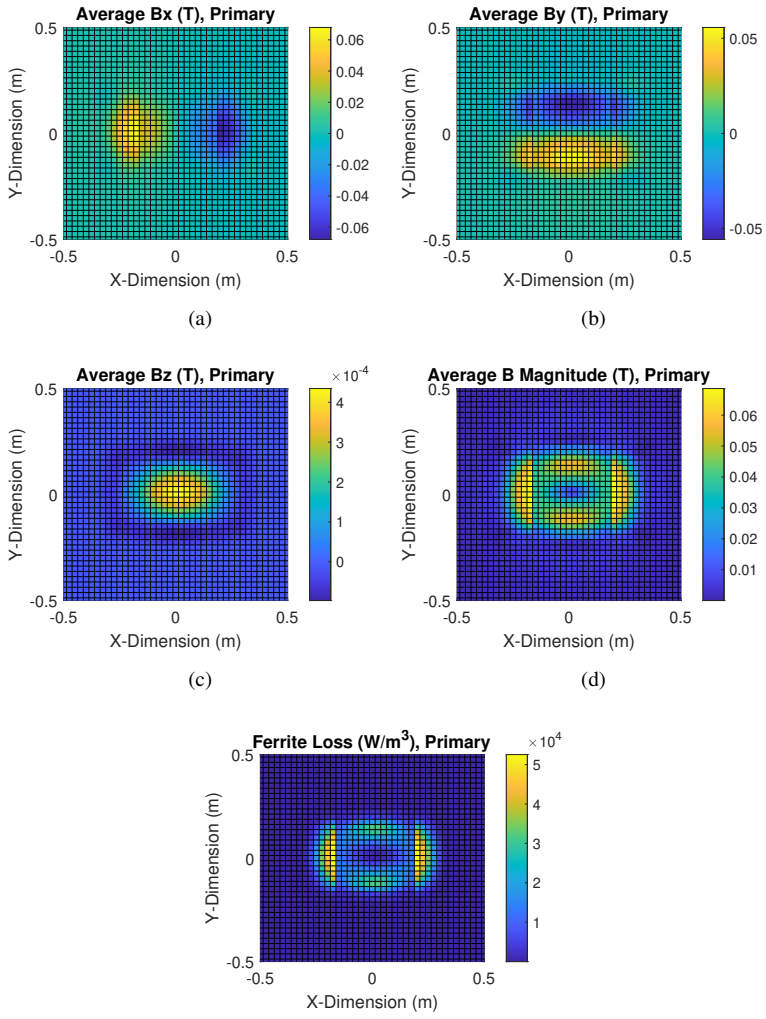

Fig. 10. (a) Average RMS fields in primary ferrite coil with a current of 17.3A in the (a) x-direction, (b) y-direction, and (c) z-direction. (d) The RMS magnitude of the ferrite flux. (e) The spatial specific power loss of the primary coil ferrite at 85 kHz. Here the inner ferrite is 5 mm and the outer ferrite is 2.7 mm, leading to lower peak fields and lower specific power loss in the middle section.

well under the saturation flux density of the material. The losses are also a function of ferrite temperature, T_{fer}. Many ferrite materials have lower losses when operating at temperatures well above room temperature. For the Ferroxcube 3C95 material, an operating temperature of 25 ^{o}C increases the loss by 16% relative to the nominal level given by the Steinmetz parameters at 85 ^{o}C [23].

To evaluate (38), the spatial flux density in the ferrites must be calculated. In the Fourier Analysis Method, this is conveniently done by taking the integral of each field component to the distance of $\mu_{fer}t_{fer}$ in the z-direction to yield the average flux density in the ferrite of a thickness of t_{fer} and relative permeability μ_{fer}. For a coil in the x-y plane, the average flux density in each direction are

$$B_{x,fer}(x,y) = \sum_{m=1}^{2N-1}\sum_{n=1}^{2N-1} \frac{-\mu_0 j k_x \psi(k_x,k_y) e^{j(k_x x + k_y y)}}{\gamma t_{fer}} \cdot (1 - e^{-\gamma t_{fer}\mu_r}) \tag{39}$$

$$B_{y,fer}(x,y) = \sum_{m=1}^{2N-1}\sum_{n=1}^{2N-1} \frac{-\mu_0 j k_y \psi(k_x,k_y) e^{j(k_x x + k_y y)}}{\gamma t_{fer}} \cdot (1 - e^{-\gamma t_{fer}\mu_r}) \tag{40}$$

$$B_{z,fer}(x,y) = \sum_{m=1}^{2N-1}\sum_{n=1}^{2N-1} -\mu_0 \psi(k_x,k_y) e^{j(k_x x + k_y y)} \cdot (1 - e^{-\gamma t_{fer}\mu_r}). \tag{41}$$

Then the average peak flux density in the ferrite, $B_{avg,fer}(x,y)$, is computed as the vector sum of the field components.

$$B_{avg,fer}(x,y) = \sqrt{\left(B_{x,fer}(x,y)\right)^2 + \left(B_{y,fer}(x,y)\right)^2 + \left(B_{z,fer}(x,y)\right)^2} \tag{42}$$

An example of this calculation is seen in Fig. 10 for the prototype coil in Fig. 12(a) with a primary current of 17.3 A at 85 kHz. In this coil, two different thicknesses of ferrite were used: 2.7 mm on the outside and 5 mm on the inside. This leads to lower flux density and less loss in the middle of the coil, where there is is more flux compared to the outside, while reducing the overall weight of ferrite similar to the approach of [10].

D. Inverter and Rectifier Losses

In the WPT system, a high-frequency full-bridge inverter drives the primary resonant tank. The secondary side is connected to a full-wave diode rectifier. In a full-bridge inverter, the primary RMS current I_1 will flow through two device on-state resistances R_{DS} for most of the switching period. Therefore, the conduction loss of the switching devices is

$$P_{R_{DS}} = 2I_1^2 R_{DS}. \tag{43}$$

The switching losses of the inverter are minimized by operating slightly above resonance so that the inverter is soft-switching. Therefore, the switching losses of the inverter and dynamic effects on R_{DS} are not included.

Likewise, on the secondary side, the secondary RMS current I_2 will flow through the forward voltages of the diodes V_f and diode resistances R_f of the rectifier. The reverse-recovery losses of the diodes are negligible as Schottky diodes are used.

$$P_{diode} = 2V_f I_{2,avg} + 2I_2^2 R_f \tag{44}$$

The average diode forward current is calculated by

$$I_{2,avg} = \frac{2\sqrt{2}}{\pi} I_2. \tag{45}$$

E. Compensation Component Losses

Power capacitors such as the ones used in the WPT system are designed to have low series resistance and dielectric loss. The ratio of real power, or loss in this case, to reactive power is expressed as the tangent of the angle ϕ of the vector sum of the real power loss P_c and reactive power Q_c in the capacitor, or the dissipation factor (DF). The real power loss of resonant capacitors is comprised of both dielectric and conduction losses. For polypropylene-based capacitors, the dielectric component of the dissipation factor remains constant with frequency

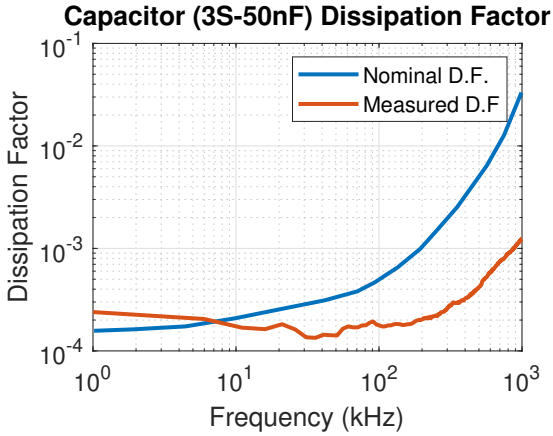

Fig. 11. The frequency-dependent loss tangent of polypropylene (PP) capacitors as in [24] compared to the measured DF of the HC1 capacitor bank with 3, 50 nF capacitors in series.

at around 10^{-4} to 2×10^{-4}. The conduction loss component of the loss tangent, however, scales with frequency such that the total loss tangent increases with frequency as illustrated in Fig. 11. Here, the measured dissipation factor of the capacitors is about half of the nominal curve given by the manufacturer at 85kHz. The equivalent series resistance (ESR) of the resonant capacitors R_C and the total power loss P_c are

$$R_C = \frac{\tan\phi(f)}{\omega C} \tag{46}$$

$$P_c = I_1^2 R_{C1} + I_2^2 R_{C2} \tag{47}$$

F. Series-Series System Circuit Model

With an equivalent AC load resistance on the secondary side R_L, the fundamental frequency model of a pair of series-tuned WPT coils is

$$\begin{bmatrix} V_1 \\ 0 \end{bmatrix} = \begin{bmatrix} Z_1 & -j\omega M \\ -j\omega M & Z_2 \end{bmatrix} \begin{bmatrix} I_1 \\ I_2 \end{bmatrix}. \tag{48}$$

where the primary and secondary lumped series impedances are, respectively

$$Z_1 = 2R_{DS} + R_{C1} + R_{11} + j\omega L_1 + 1/(j\omega C_1) \tag{49}$$

$$Z_2 = 2R_f + R_{C2} + R_{22} + R_L + j\omega L_2 + 1/(j\omega C_2). \tag{50}$$

The AC input voltage V_1 and equivalent AC load resistance R_L are found by the first-harmonic approximation of a square wave as a function of the DC input voltage $V_{1,DC}$ and the DC output load resistance $R_{L,DC}$.

$$R_L = \frac{8}{\pi^2} R_{L,DC} \tag{51}$$

$$V_1 = \frac{4}{\pi} V_{1,DC} \tag{52}$$

(a) (b) (c)

Fig. 12. (a). Prototype 6.6 kW coil. (b) Overall experimental setup. (c) Resonant capacitor bank.

Likewise, the DC output voltage is

$$V_{2,DC} = \frac{\pi}{2\sqrt{2}} I_2 R_L - 2V_f. \tag{53}$$

In this linear circuit model, the resistances due to the ferrite losses are neglected. In the final loss calculation, the ferrite losses are calculated from the currents found by this linear model. By inverting this matrix, the input impedance of the system seen by the inverter is

$$Z_{in} = \frac{Z_1 Z_2 + (\omega M)^2}{Z_2}. \tag{54}$$

To assure the zero-voltage switching of the inverter switches, the frequency and load of the WPT system are chosen so that the input impedance of the primary coil is inductive by choosing an operating frequency slightly greater than the resonant frequency of the tanks.

IV. Experimental Results

A 6.6 kW prototype was built to evaluate one of the candidate coil geometries in Fig. 9(a) and validate the loss and field models with experimental measurements. The parameters used to model the system performance are given in Table I. The overall system consists of a set of two matched planar coils, two compensation capacitor banks, and power electronics consisting of a full-bridge inverter with four MOSFETs and gate driver boards, a control board with an FPGA, and a full-bridge diode rectifier.

One of the two identical prototype coils is shown in Fig. 12(a). Each coil is a sandwich structure comprised, from top to bottom, of a polycarbonate coil former, ferrite tiles of two thicknesses, hardboard spacers, and an aluminum sheet held together with nylon bolts and reinforced tape. The total length of the wire in each coil was measured to be 29.8 m, with 24.8 m in the coils themselves. The calculated length of the contours was 24.8 m. The additional length is accounted for in the loss model. The airgap holder in Fig. 12(b) was made out of wood and nylon bolts to suspend one of the coils at different airgaps. The four threaded nylon rods allow for the quick adaptation of the airgap and support the upper coil from the bottom. Litz wire was used to symmetrically wind the coils.

The compensation capacitors are constructed of high-density resonant capacitors from Illinois Capacitor. Due to the need to reach high voltage levels, three capacitors were placed in series as seen in Fig. 12(c). An identical bank was constructed and connected to the secondary side to provide series-series tuning for the system. The area

TABLE I

LOSS MODEL PARAMETER DEFINITIONS AND VALUES

Parameters		Value
Ferrite Steinmetz Parameters Ferroxcube 3C95		$\mu_r = 3000$ $C_m = 92.1\text{e-}3$ mW/cm^3 $\alpha = 1.045$ $\beta = 2.440$
Ferrite Temperature Coefficients Ferroxcube 3C95		$C_t = 1.332$ $C_{t1} = 0.0079$ $C_{t2} = 4.62\text{e-}5$
Steady-State Temperature of Ferrite		$T_{fer} = 20$°C
Ferrite Thickness		$t_{fer} = 2.7$ mm (outer) $t_{fer} = 5$ mm (inner)
Litz Wire	Outer Diameter Number of Strands Strand Diameter Operations Wire Length	$d_{out} = 3.8$ mm $n = 1100$ $d_{str} = 0.0787$ mm $N_b = 1$ $N_c = 2$ $L_T = 29.8$ m
Compensation Capacitor		$\tan\delta$ see Fig. 11
Inverter On-Resistance NVHL040N120SC1		$R_{DS} = 45$ mΩ
Diode Model Curve Fit STPSC40H12CWL		$V_f = 0.913$ V $R_f = 36.6$ mΩ /2
Temperature Coefficient, Copper		$C_{Cu,t} = +0.393$ %/°C
Steady-State Temp. of Copper		$T_{Cu} = 38$ °C
Gap Between Ferrite and Wire Plane		$z_g = 7.5$ mm

between the nuts on the underside of the capacitors required additional voltage insulation where the corners of nuts were facing each other. To resolve this issue, FR4 fins placed on top of Mylar tape were made to provide additional voltage insulation between the capacitor nuts. These are held in place by long pieces of FR4 aligning the busbars and nylon bolts. The assembly is enclosed in a PVC and plexiglass box.

A. Impedance Measurements

In Table II, the measured and calculated inductances of the system are compared. The measurements were obtained with an Agilent Technologies E4990A impedance analyzer. As measured, the self-inductance of the coils change as a function of airgap due to the presence of ferrite across the airgap as also seen in [25]. The FAM model also captures this effect. This change in self-inductance slightly changes the resonant frequency of the tank. To account for this effect, the operating frequency is chosen such that the input impedance is inductive for the largest airgap,

TABLE II

CALCULATED INDUCTANCE VALUES VS. MEASUREMENTS

Airgap	Param.	FEA	FAM	Measured	Error, FAM to Meas. (%)
125 mm	L_1, L_2	216.1 µH	224.9 µH	218.9 µH, 217.2 µH	2.7%, 3.5%
	M	75.2 µH	82.6 µH	79.9 µH	3.3%
210 mm	L_1, L_2	203.2 µH	204.5 µH	205.4 µH, 203.8 µH	-0.4%, 0.3%
	M	29.8 µH	31.9 µH	30.2 µH	5.3%
250 mm	L_1, L_2	201.7 µH	201.7 µH	200.3 µH, 199.7 µH	0.7%, 1.0%
	M	20.3 µH	21.7 µH	20.0 µH	7.8%

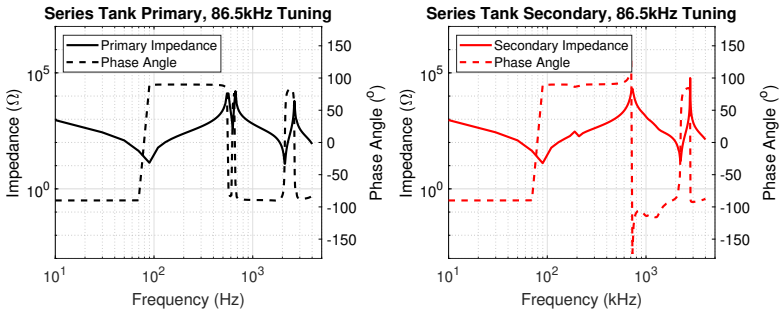

(a) (b)

Fig. 13. Tank Impedance of the (a) primary and (b) secondary tanks at 86.5 kHz tuning.

when the coil self-inductances are lowest and the tank resonant frequency is the highest. The airgap used in this document is defined as the magnetic airgap of the system, i.e. the distance between the ferrites of each coil.

In Fig. 13, the measured series impedances of the primary and secondary tanks are shown when tuned to the 86.5 kHz operating points with three 50 nF capacitors in series. The parasitic series resonances of the tanks were seen to produce a high-frequency resonant point, as seen in the later test results.

B. Efficiency Measurements and Waveforms

Tests were run to validate the efficiency and loss models over misalignment. Two power supplies were used in the tests: a Keysight N8935A for the high-power tests at 125mm at 3.4kW and 210mm at 6.7kW at alignment and a BK Precision PVS60085MR for the other low-power tests. A BK Precision 8612 electronic load was used alone or in parallel with wirewound resistors for these low-power tests. For the high-power tests, the wirewound resistor bank alone was used. Because of the voltage and current limitations of the electronic load and power supply for the low-power tests, the power levels are limited to 1.1 kW and below at 250mm and at 125mm and 210mm in misaligned conditions. The system waveforms were obtained with a Tektronix MSO4104B-L. The DC current and voltage measurements used to derive DC-DC efficiency were obtained by multimeter and power supply current measurements. For these tests, the system was run in open-loop with constant load resistance.

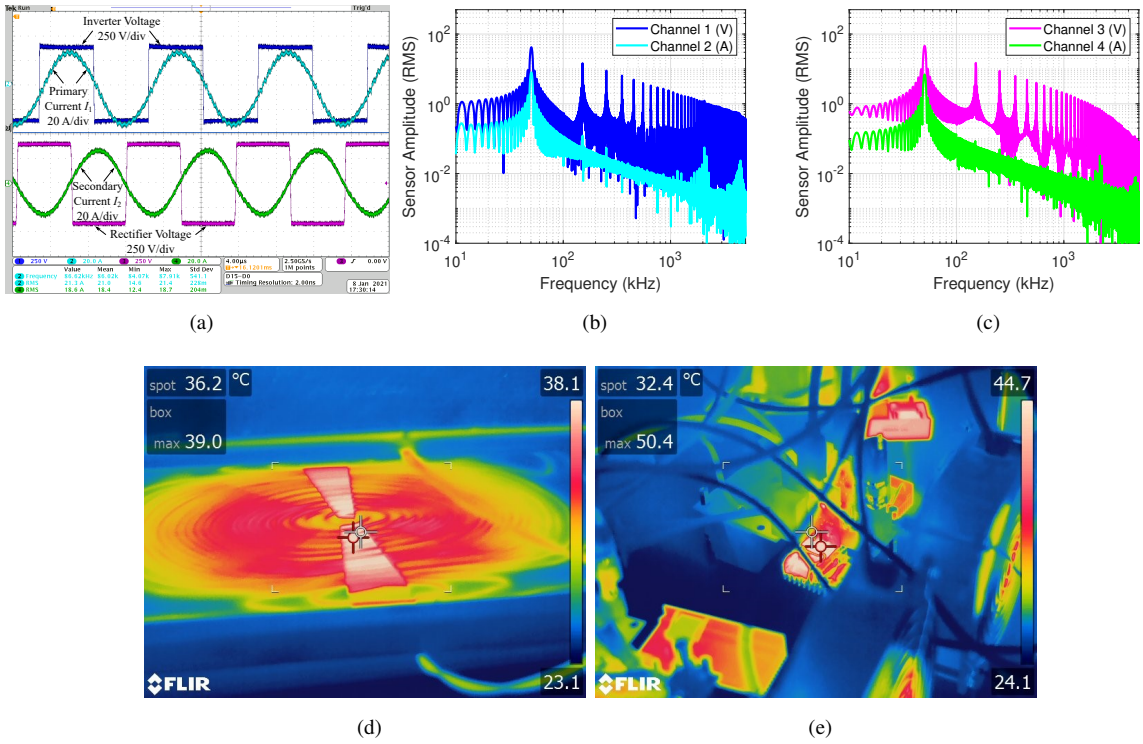

(a) (b) (c)

(d) (e)

Fig. 14. Experimental results at 6.7 kW and 86 kHz, 210 mm at alignment. (a) Waveforms of switch node voltages and currents. CH1: Blue primary switch node voltage (250 V/div), CH2: cyan primary current I_1 (20 A/div), CH3: magenta secondary switch node voltage (250 V/div), and CH4: green secondary current I_2 (20 A/div). (b) Frequency components of CH1 and CH2. (c) Frequency components of CH3 and CH4. (d) Thermal image of secondary coil showing a maximum wire temperature of 39 °C. (e) Thermal image of the inverter (top) and rectifier (bottom) heat sinks.

The waveforms of the system at 210 mm and 6.7 kW are shown in Fig. 14(a). The frequency components of the waveforms are also given in Fig. 14(b)-14(c), showing the square-wave harmonics of the inverter and rectifier voltages and coil currents. The effect of the parasitic resonances of the tanks in Fig. 13 is seen in high-frequency components of the current waveforms. At the 6.7 kW operating point, the temperatures of the system elements were captured by thermal camera as shown in Fig. 14(d)-14(e). These temperatures were used to determine loss model parameters in Table I. The modeled loss breakdown of the system and efficiency measurements over varying misalignments are shown in Fig. 15. In these figures, the loss models matched the experimental measurements well over varying misalignments.

A summary of the measured efficiency values are given in Table III. As shown, the efficiency of this work is similar to the previous works summarized in Table VI when compared by the airgap divided by the geometric mean length (GML) of the coil dimensions similar to the metric proposed in [26].

C. Field Measurements

A sensor cubic similar to [4] was made to measure the fields of the system during operation for comparison with model values. The voltages induced in the sensor windings were measured with a Tektronix MDO3104 oscilloscope.

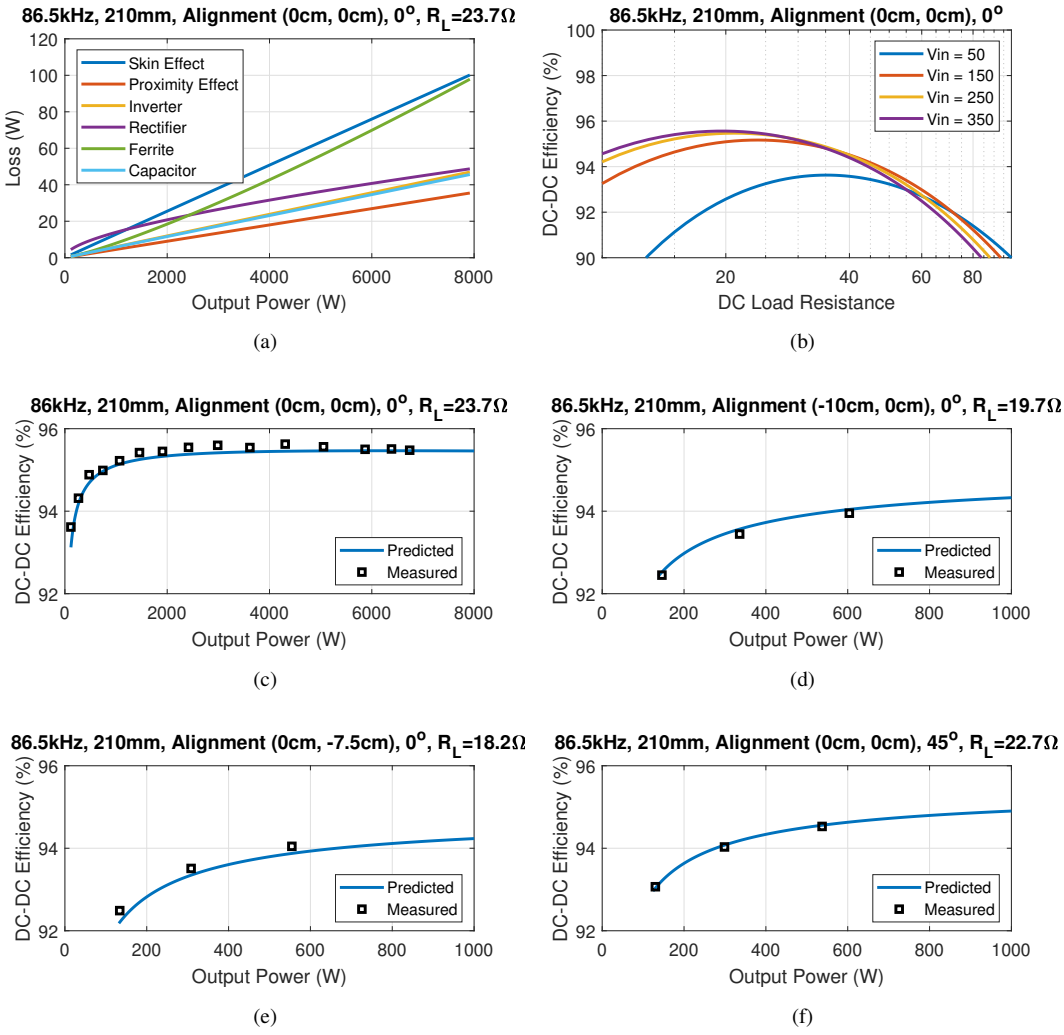

Fig. 15. (a) Modeled loss breakdown of the system at alignment over varying output resistances. (b) Modeled efficiency of system over load resistance at alignment. (c) Model efficiency vs. measured efficiency at alignment, (d) at -10 cm in the X-direction, (e) at -7.5 cm in the Y-direction, and (f) at 45° rotation.

TABLE III

PEAK MEASURED DC/DC EFFICIENCIES AT 86.5KHZ

Airgap	Misalignment (X,Y)			
	0 cm, 0 cm	-10 cm, 0 cm	0 cm, -7.5 cm	45°
125 mm	97.6%	96.6%	96.3%	97.0%
210 mm	95.6%	94.0%	93.0%	94.5%
250 mm	93.1%	91.4%	90.9%	92.4%

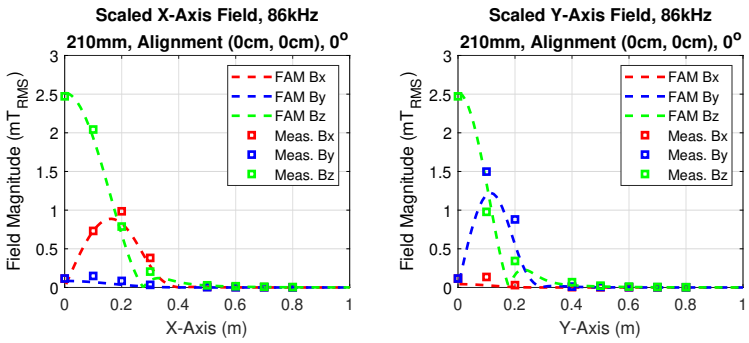

(a) (b)

Fig. 16. Scaled field measurements and model outputs at 86.5 kHz, 210 mm, and 6.6 kW. (a) Fields on the X-axis and (b) the Y-axis.

TABLE IV
SENSOR CUBIC VALUES

Parameter	Value	
Magnet Wire AWG	30 AWG	
Number of Turns	$N = 45$ turns	
Turn Area	$A = 23.04$ cm^2	
Field Sensitivity (dV/dB)	86.5 kHz	56.4 mV/μT
RC Filter Values	R =1.6 kΩ $C = 300$ pF	
RC Corner Frequency	300 kHz	

Due to the high-frequency self-resonance of the sensor windings, an RC filter was used to damp the high-frequency voltages and is included in the calculation of the stray field. The parameters of the cubic and RC-filter are given in Table IV. Field measurements at the center of a 210mm airgap are shown in Fig. 16. Here, the FAM field models match the experiment with some accuracy, especially for the B_z values. The B_x and B_y values were affected by the accuracy of positioning the sensor cubic height between the coils. These measurements were taken at a DC output power of 474 W to limit the voltages induced in the sensor windings from the large fields within the coil extents. The measurements are scaled by the square root of the ratio of 6.6 kW to 474 W.

The measured stray fields at 80 cm are summarized in Table V. The field measurements at misalignment are on the side closest to the misaligned secondary. Compared to the literature on a normalized basis of stray field divided by the square root of output power, the measured stray fields at 80 cm were less than the works summarized in Table VI and well below the ICNIRP 27 μT limit. In Table VI, the stray field metric μT/kW$^{0.5}$ comes from the direct relationship between the coil currents and field magnitude and the coil to coil power equation, $P = \omega M I_1 I_2$, where the power is proportional to the product of the coil currents. This relationship allows the stray fields of systems operating at different power levels to be compared and for the scaling of stray field measurements to higher or

TABLE V

SUMMARY OF SCALED RMS FIELD MEASUREMENTS (X,Y) AT 0.8 M, 86.5 KHZ AND 6.6 KW

Airgap	Misalignment (X,Y)		
	0 cm, 0 cm	-10 cm, 0 cm	0 cm, -7.5 cm
125 mm	1.8 μT, 1.4 μT	4.5 μT, 1.8 μT	2.1 μT, 3.1 μT
210 mm	4.4 μT, 3.6 μT	6.6 μT, 4.2 μT	4.5 μT, 5.6 μT
250 mm	6.5 μT, 4.5 μT	8.9 μT, 5.3 μT	6.6 μT, 7.2 μT

TABLE VI

COMPARISON OF WPT SYSTEMS IN THE LITERATURE AND THE PROTOTYPE

Ref.	Power Level	Coil Dimension	Airgap (mm)	Airgap/ GML	Stray Field 80 cm - X, Y	Stray Field Metric $\mu T/kW^{0.5}$	DC/DC Efficiency	Freq. (kHz)	Coil Shape
[4]	50 kW	76 cm x 41 cm	160	(0.29)	N/A, 22.5 μT	(N/A, 3.2)	95.8%	85	Rect.
[4]	50 kW	76 cm x 41 cm	160	(0.29)	N/A, 12.5 μT	(N/A, 1.8)	95.3%	85	DD
[8], [27]	120 kW	88 cm x 67 cm	125	(0.16)	19.1 μT, 12.3 μT (11 kW)	(5.8, 3.7)	97.1%	25	DD
[28]	50kW	54 cm x 47 cm	150	(0.30)	N/A, 34.7 μT	(N/A, 4.9)	95.1%	85	3Φ-DD
This Work	6.6 kW	71 cm x 54 cm	125 210 250	(0.20) (0.34) (0.41)	1.8 μT, 1.4 μT 4.4 μT, 3.6 μT 6.5 μT, 4.5 μT	(0.7, 0.5) (1.7, 1.4) (2.5, 1.8)	97.6% 95.5% 93.1%	86.5	Shielded Rect.

lower power levels as done in this work.

V. CONCLUSION

In this work, the Fourier Analysis Method (FAM) was used to predict the system efficiency, inductances, fields, and performance of complex, symmetric planar coil geometries derived from an optimization of Fourier basis function coefficients. The optimization outputs are geometries that meet the stray field and power level constraints with minimum current. The FAM is then used to estimate the efficiency over various number of turns, conductor sizes, and ferrite thicknesses over varying airgaps and misalignments.

A 6.6 kW WPT prototype with a shielded rectangular coil geometry was built from an optimization output to validate the method. The prototype was tested over a range of misalignments and airgaps to test the inductance, field, and loss models. As shown in Table VI, the prototype achieved similar efficiency with lower stray field when compared to the literature by a metric of the airgap over the geometric mean length (GML) of the coils and a metric of stray field over the square root of output power. Improving the efficiency and stray field is essential to achieve high-power inductive charging for EVs that complies with stray field and EMI limits. In future work, thermal effects and cooling will be considered in tandem with the loss models to design and validate a higher-power WPT system.

ACKNOWLEDGMENT

The authors would like to thank Bob Martin and Caden Webb for their assistance with the material procurement, manufacture, and setup of the experimental system.

REFERENCES

[1] A. Foote, D. Costinett, R. Kusch, J. Pries, M. Mohammad, and B. Ozpineci, "Fourier analysis method for wireless power transfer coil design," in *2020 IEEE 21st Workshop on Control and Modeling for Power Electronics (COMPEL)*, 2020, Conference Proceedings, pp. 1–8.

[2] International Commission on Non-Ionizing Radiation Protection, "Guidelines for limiting exposure to time-varying electric and magnetic fields (1 Hz to 100 kHz)," *Health Physics*, vol. 99, no. 6, pp. 818–836, 2010.

[3] IEC, "CISPR 11: Industrial scientific and medical equipment - Radiofrequency disturbance characteristics - Limits and methods of measurement," June 2016.

[4] R. Bosshard, U. Iruretagoyena, and J. W. Kolar, "Comprehensive evaluation of rectangular and Double-D coil geometry for 50 kW/85 kHz IPT system," *IEEE Journal of Emerging and Selected Topics in Power Electronics*, vol. 4, no. 4, pp. 1406–1415, 2016.

[5] T. Campi, S. Cruciani, F. Maradei, and M. Feliziani, "Active coil system for magnetic field reduction in an automotive wireless power transfer system," in *2019 IEEE International Symposium on Electromagnetic Compatibility, Signal and Power Integrity (EMC+SIPI)*, 2019, Conference Proceedings, pp. 189–192.

[6] M. Lu and K. D. T. Ngo, "Circuit models and fast optimization of litz shield for inductive-power-transfer coils," *IEEE Transactions on Power Electronics*, vol. 34, no. 5, pp. 4678–4688, 2019.

[7] M. Mohammad, M. S. Haque, and S. Choi, "A litz-wire based passive shield design to limit EMF emission from wireless charging system," in *2018 IEEE Energy Conversion Congress and Exposition (ECCE)*, 2018, Conference Proceedings, pp. 97–104.

[8] M. Mohammad, J. Pries, O. Onar, V. P. Galigekere, G. Su, S. Anwar, J. Wilkins, U. D. Kavimandan, and D. Patil, "Design of an EMF suppressing magnetic shield for a 100-kW DD-coil wireless charging system for electric vehicles," in *2019 IEEE Applied Power Electronics Conference and Exposition (APEC)*, 2019, Conference Proceedings, pp. 1521–1527.

[9] B. Zhang, R. B. Carlson, V. P. Galigekere, O. C. Onar, and J. L. Pries, "Electromagnetic shielding design for 200 kW stationary wireless charging of light-duty EV," in *2020 IEEE Energy Conversion Congress and Exposition (ECCE)*, 2020, Conference Proceedings, pp. 5185–5192.

[10] M. Mohammad, S. Choi, Z. Islam, S. Kwak, and J. Baek, "Core design and optimization for better misalignment tolerance and higher range of wireless charging of PHEV," *IEEE Transactions on Transportation Electrification*, vol. 3, no. 2, pp. 445–453, 2017.

[11] M. Lu and K. D. T. Ngo, "Analytical calculation of proximity-effect resistance for planar coil with litz wire and ferrite plate in inductive power transfer," *IEEE Transactions on Industry Applications*, pp. 1–1, 2019.

[12] G. N. Peeren, "Stream function approach for determining optimal surface currents," Thesis, Eindhoven University of Technology, 2003.

[13] M. Poole, P. Weiss, H. S. Lopez, M. Ng, and S. Crozier, "Minimax current density coil design," *Journal of Physics D: Applied Physics*, vol. 43, no. 9, 2010.

[14] M. Landreman, "An improved current potential method for fast computation of stellarator coil shapes," *Nuclear Fusion*, vol. 57, no. 4, 2017.

[15] J. R. Melcher, *Continuum Electromechanics*. MIT press Cambridge, 1981, vol. 2.

[16] B. L. J. Gysen, K. J. Meessen, J. J. H. Paulides, and E. A. Lomonova, "General formulation of the electromagnetic field distribution in machines and devices using Fourier analysis," *IEEE Transactions on Magnetics*, vol. 46, no. 1, pp. 39–52, 2010.

[17] Z. Luo and X. Wei, "Analysis of square and circular planar spiral coils in wireless power transfer system for electric vehicles," *IEEE Transactions on Industrial Electronics*, vol. 65, no. 1, pp. 331–341, 2018.

[18] J. P. C. Smeets, T. T. Overboom, J. W. Jansen, and E. A. Lomonova, "Three-dimensional magnetic field modeling for coupling calculation between air-cored rectangular coils," *IEEE Transactions on Magnetics*, vol. 47, no. 10, pp. 2935–2938, 2011.

[19] C. Feeney, J. Zhang, and M. Duffy, "AC winding loss of phase-shifted coupled windings," *IEEE Transactions on Power Electronics*, vol. 31, no. 2, pp. 1472–1478, 2016.

[20] M. K. Kazimierczuk, *High-frequency magnetic components*. John Wiley and Sons, 2009.

[21] J. Mühlethaler, "Modeling and multi-objective optimization of inductive power components," PhD Dissertation, ETH Zürich, Zürich, Switzerland, 2012.

[22] New England Wire, "Litz wire technical information," https://www.newenglandwire.com/, 2003.

[23] Ferroxcube, "Power conversion materials," https://www.ferroxcube.com, 2020.

[24] Illinois Capacitor, "Metallized polypropylene film capacitors data," https://www.illinoiscapacitor.com/, 2020.

[25] S. Y. Jeong, J. H. Park, G. P. Hong, and C. T. Rim, "Autotuning control system by variation of self-inductance for dynamic wireless EV charging with small air gap," *IEEE Transactions on Power Electronics*, vol. 34, no. 6, pp. 5165–5174, 2019.

[26] A. L. Stein, P. A. Kyaw, and C. R. Sullivan, "Figure of merit for resonant wireless power transfer," in *2017 IEEE 18th Workshop on Control and Modeling for Power Electronics (COMPEL)*, 2019, Conference Proceedings, pp. 1–7.

[27] V. P. Galigekere, J. Pries, O. C. Onar, G. Su, S. Anwar, R. Wiles, L. Seiber, and J. Wilkins, "Design and implementation of an optimized 100 kW stationary wireless charging system for EV battery recharging," in *2018 IEEE Energy Conversion Congress and Exposition (ECCE)*, 2018, Conference Proceedings, pp. 3587–3592.

[28] J. Pries, V. P. N. Galigekere, O. C. Onar, and G.-J. Su, "A 50-kW three-phase wireless power transfer system using bipolar windings and series resonant networks for rotating magnetic fields," *IEEE Transactions on Power Electronics*, vol. 35, no. 5, pp. 4500–4517, 2020.